1 **Exploring the ocean mesoscale at reduced computational cost with FESOM 2.5: efficient**
2 **modeling strategies applied to the Southern Ocean**

3 Nathan Beech[1], Thomas Rackow[2], Tido Semmler[3], and Thomas Jung[1,4]

4 1. Alfred Wegener Institute Helmholtz Center for Polar and Marine Research, Bremerhaven,
5 Germany

6 2. European Center for Medium-range Weather Forecasts, Bonn, Germany

7 3. Met Eireann, the Irish Meteorological Service, Dublin, Ireland

8 4. Department of Physics and Electrical Engineering, University of Bremen, Bremen, Germany

9 Corresponding Author: Nathan Beech (Nathan.beech@awi.de)

10

11   **Abstract**

12   Modeled projections of climate change typically do not include a well-resolved ocean mesoscale

13   due to the high computational cost of running high-resolution models for long time periods. This

14   challenge is addressed using efficiency-maximizing modeling strategies applied to 3 km simulations of

15   the Southern Ocean in past, present, and future climates. The model setup exploits reduced-resolution

16   spin-up and transient simulations to initialize a regionally refined, high-resolution ocean model during

17   short time periods. The results are compared with satellite altimetry data and more traditional eddy-

18   present simulations and evaluated based on their ability to reproduce observed mesoscale activity and to

19   reveal a response to climate change distinct from natural variability. The high-resolution simulations

20   reproduce the observed magnitude of Southern Ocean eddy kinetic energy (EKE) well, but differences

21   remain in local magnitudes and the distribution of EKE. The coarser, eddy-permitting ensemble simulates

22   a similar pattern of EKE, but underrepresents observed levels by 55%. At approximately 1 °C of

23   warming, the high-resolution simulations produce no change in overall EKE, in contrast to full ensemble

24   agreement regarding EKE rise within the eddy-permitting simulations. At approximately 4 °C of

25   warming, both datasets produce consistent levels of EKE rise in relative terms, although not absolute

26   magnitudes, as well as an increase in EKE variability. Simulated EKE rise is concentrated where flow

27   interacts with bathymetric features in regions already known to be eddy-rich. Regional EKE change in the

28   high-resolution simulations is consistent with changes seen in at least four of five eddy-permitting

29   ensemble members at 1 °C of warming, and all ensemble members at 4 °C. However, substantial noise

30   would make these changes difficult to distinguish from natural variability without an ensemble.

31   **Plain Language Summary**

32   Cost-reducing modeling strategies are applied to high-resolution simulations of the Southern

33   Ocean in a changing climate. They are evaluated with respect to observations and traditional, lower-

34   resolution modeling methods. The simulations effectively reproduce small-scale ocean flows seen in

35   satellite data and are largely consistent with traditional model simulations after 4 °C of warming. Small-

36   scale flows are found to intensify near bathymetric features and to become more variable.

1 Introduction

Mesoscale activity in the Southern Ocean has been the subject of much research and interest in recent years due to the intensification of Southern Hemisphere westerlies (Marshall, 2003), the phenomena of eddy saturation and compensation (Munday et al., 2013; Bishop et al., 2016), and the potential for carbon sequestration in the face of ongoing anthropogenic emissions (Sallée et al., 2012; Landschützer et al., 2015; Frölicher et al., 2015). Satellite observations already reveal an intensification of eddy activity in the Antarctic Circumpolar Current (ACC) and changes are attributed primarily to wind stress (Marshall, 2003; Hogg et al., 2015; Martínez-Moreno et al., 2021). Modeling studies have been able to reproduce the observed changes, as well as project continued intensification throughout the 21st century (Beech et al., 2022), but the modeled results rely on only partially resolved eddy activity relative to observations, leaving open the possibility for new findings or greater clarity.

Advances in computational capabilities have enabled ocean modeling science to make great progress in overcoming the substantial computational burden of simulating the mesoscale. However, shortcomings remain, particularly in the Southern Ocean where the Rossby radius can be as small as 1 km, increasing the computational cost of resolving eddies (Hallberg, 2013). Even model resolutions that can generally be considered eddy-resolving are only eddy-permitting poleward of 50° if grid spacing does not vary in space (Hewitt et al., 2020). This highlights an efficiency challenge in simulating the mesoscale with traditional model grids; resolutions necessary to resolve high-latitude, small-radius eddies are both prohibitively expensive and unnecessary to resolve mesoscale eddies in the lower latitudes. Fortunately, a growing number of modeling alternatives to traditional grids now enable dynamic spatial allocation of resources (Danilov, 2013; Ringler et al., 2013; Danilov et al., 2017; Jungclaus et al., 2022), creating the opportunity to more efficiently resolve the mesoscale.

As resource allocation in high-resolution modeling becomes spatially flexible in the pursuit of more efficient configurations, the temporal component must also be scrutinized for efficiency. Traditional modeling approaches require long spin-up periods in order to equilibrate the deep ocean and reduce

4

62   model drift (Irving et al., 2021). Although the impacts of drift are not negligible, they generally affect

63   large-scale processes in the deep ocean; mesoscale processes that require high resolutions to simulate are

64   typically fast-to-equilibrate and will appear relatively quickly wherever large-scale ocean conditions lead

65   to their creation. Admittedly, one cannot entirely disentangle the two scales, as mesoscale activity does

66   affect the position of fronts, stratification, and the paths of ocean circulation (Marshall et al., 2002;

67   Marzocchi et al., 2015; Chassignet and Xu, 2017). Yet, with equilibration times for the deep ocean on the

68   scale of thousands of years (Irving et al., 2021), the possibility, and ultimately necessity, to reduce the

69   resolution of spin-up runs relative to production runs must be investigated.

70   Advancing the concept of dynamic temporal allocation of resources further, the traditional

71   transient climate change simulation also represents an efficiency bottleneck for some applications; by

72   modifying the climate continuously in time, each year of a transient simulation is effectively a single

73   realization of a global mean climatic state that varies from the following and preceding years by only a

74   fraction of a degree. For some applications, like hindcasts of real events or trend analysis, this approach

75   may be desirable, but for assessing the impacts of climate change with limited resources and a low signal-

76   to-noise ratio, a larger sample of realizations for a consistent climatic state may be more suitable.

77   Aside from oceanic concerns, the atmosphere can have substantial impacts on mesoscale activity

78   in climate models. Most simply, with a coupled atmosphere, absolute surface winds will react to ocean

79   eddy activity, whereas atmospheric forcing will not, resulting in more eddy killing by wind stress

80   (Renault et al., 2016). Additionally, an atmosphere coupled to a high-resolution ocean must be of

81   similarly high resolution for certain mesoscale interactions to be resolved (Byrne et al., 2016). Ultimately,

82   the modeled atmosphere further escalates the already exponential cost of increasing ocean resolution by

83   requiring more computational resources in order for the benefits of the resolved mesoscale to fully

84   transfer to the broader climate.

85   To address the computational inefficiencies outlined above, a novel simulation configuration is

86   proposed, combining several experimental modeling approaches. Simulations will exploit the multi-

87   resolution Finite volumE Sea-ice Ocean Model (FESOM) (Danilov et al., 2017) employing a high-

88   resolution unstructured mesh that concentrates computational resources on the Southern Ocean, while

89   maintaining grid resolution in the remainder of the global ocean that can still be considered high-

90   resolution, as in, for example, HighResMIP (Haarsma et al., 2016). The multi-resolution strategy

91   overcomes the efficiency challenges of resolving high-latitude eddies without needlessly increasing

92   tropical resolutions, as well as limiting the focus and computational requirements to one hemisphere. The

93   high-resolution simulations will make use of a spin-up simulation on a medium-resolution, eddy-

94   permitting mesh to avoid the computational burden of allowing an eddy-resolving ocean to equilibrate

95   deep, slow-changing processes. The eddy-permitting mesh will also be used to simulate the transient

96   periods between shorter, high-resolution time slices, increasing the signal-to-noise ratio of the results by

97   separating the production data further in time and the progression of anthropogenic climate change.

98   Finally, the ocean model will be forced with atmospheric data from existing coupled simulations

99   (Semmler et al., 2020). Although this will not facilitate mesoscale atmosphere-ocean interaction, the

100 simulation will reflect the climatic development of an eddy-permitting simulation of the future

101 atmosphere without the additional computational requirements.

102   The Southern Ocean is one of the world's hotspots for mesoscale activity and a region where

103 substantial change is anticipated in the context of anthropogenic climate change (Beech et al., 2022).

104 Simultaneously, the high latitude of the region makes eddy-resolving model simulations computationally

105 demanding and observational data relatively scarce (Auger et al., 2023; Hallberg, 2013). Yet, as the

106 climate changes, the importance of the Southern Ocean grows as a heat and carbon sink, an ecosystem,

107 and a medium for feedback between the atmosphere and ocean (Byrne et al., 2016; Frölicher et al., 2015).

108 Thus, the study of the Southern Ocean demands innovation in the modeling field to produce high-

109 resolution simulations at reduced computational cost. This study maximizes grid resolution relative to

110 computational cost using an unstructured, multi-resolution grid, a medium-resolution spin-up simulation,

111 and atmospheric forcing from lower-resolution coupled simulations in order to focus resources as much as

112   possible on resolving mesoscale activity in the study region. The resulting simulations enable an

113   exploratory analysis of the past, present, and future of the Southern Ocean with a fully resolved

114   mesoscale. Simulations with this cost-efficient, high-resolution configuration are presented in comparison

115   to a comprehensive ensemble of eddy-permitting simulations to assess the performance of the efficiency-

116   focused approach in reproducing mesoscale activity and its response to climate change.

2   Methods

2.1 Experimental setup

119   This analysis contrasts a subset of simulations from AWI-CM-1-1-MR's contribution to the sixth

120   phase of the Coupled Model Intercomparison Project (CMIP6; Semmler et al., 2020), (hereafter referred

121   to as the AWI-CM-1 ensemble) with single-member stand-alone ocean simulations using an updated

122   version of FESOM (FESOM 2.5) and a mesh substantially refined to a resolution surpassing 3 km in the

123   Southern Ocean (hereafter referred to as the SO3 simulations) (Supplementary Figure 1). Observations of

124   ocean surface velocity derived from satellite altimetry data are also used to evaluate model performance

125   for both modeled datasets during the period of overlap with the altimetry record. The AWI-CM-1

126   simulations consist of the five-member ensemble of historical simulations and the five-member ensemble

127   of climate change projections under shared socioeconomic pathway (SSP) 3-7.0 which were performed by

128   AWI-CM-1-1-MR in CMIP6 (Semmler et al., 2020). These are state-of-the-art CMIP6 experiments and

129   benefit from the multiple ensemble members and long spin-up times that CMIP simulations typically

130   boast. However, while the AWI-CM-1 ensemble reproduces eddy activity remarkably well within the

131   context of CMIP6 (Beech et al., 2022), high-resolution ocean modeling now far surpasses even the

132   highest ocean resolutions in the CMIP6 ensemble. Conversely, the SO3 simulations push the limits of

133   ocean resolution but rely on several measures for maximizing computational efficiency that may impact

134   the robustness of the simulations. Details on the experimental setup for CMIP6 and ScenarioMIP are

135   widely available (Eyring et al., 2016; O'Neill et al., 2016) and information more specific to AWI-CM-1-

136   1-MR's contribution has been published previously (Semmler et al., 2020). The following sections will

137   outline the details of the SO3 simulations.

138   To produce initial conditions for the high-resolution model simulations on the SO3 mesh, a

139   medium-resolution, eddy-permitting, ocean-only transient simulation was first run from 1851 to 2100

140   using the same ocean mesh employed by AWI-CM-1-1-MR in CMIP6 (Semmler et al., 2020). This mesh

141   has been shown to effectively reproduce eddy activity in active regions while maintaining a

142   computational cost comparable to a traditional ¼ ° model (Beech et al., 2022). The transient simulation

143   was initialized with conditions for ocean temperature and salinity, as well as sea ice concentration,

144   thickness, and snow cover taken from the end of the first year (1850) and first ensemble member

145   (r1i1p1f1) of AWI-CM-1-1-MR's historical simulations in CMIP6 (Semmler et al., 2018, 2020, 2022a,

146   b). In this way, the model undergoes a semi-cold start in which ocean conditions are not exact

147   continuations of the previous coupled simulation, but should be far closer to equilibrium than a true cold

148   start initialization. The eddy-permitting transient simulation was forced using atmospheric data from the

149   same ensemble member of the historical CMIP6 simulations until 2014 (Semmler et al., 2022a), and

150   thereafter using the first ensemble member of AWI-CM-1-1-MR's ScenarioMIP simulations for SSP 3-

151   7.0 (Eyring et al., 2016; O'Neill et al., 2017; Semmler et al., 2022b). This approach to forcing takes

152   advantage of a coupled simulation, CMIP6, to produce a forcing dataset of better temporal and spatial

153   coverage than the observational record and which maintains a realistic transient climate throughout

154   anthropogenic impacts during the 21st century.

155   In the years 1950, 2015, and 2090, FESOM is reinitialized with the high-resolution ocean grid,

156   SO3 (Supplementary Figure 1), using the same semi-cold start approach and forcing dataset that was

157   implemented for the eddy-permitting transient simulation described previously. These years were chosen

158   to represent a historical period, beginning in 1950, when the effects of climate change on EKE should be

159   small or none (Beech et al., 2022); a near-present period, beginning in 2015, in which the simulations will

160   overlap with satellite altimetry data; and a projected period, beginning in 2090, which should include a

161   strong climate change signal. The latter two simulated periods represent 1.07 °C and 3.74 °C of warming,

162   respectively, in the first ensemble member of the AWI-CM-1 ensemble defined as a rise in the 21-year

163   running mean of global mean two-meter air temperatures. Warming of the ensemble mean is similar: 1.08

164   and 3.76 °C respectively, and warming is henceforth approximated as 1 °C and 4 °C in Fig. 4 and the text.

165   Initial conditions for these shorter time-slice simulations are taken from the end of the previous year of

166   the eddy-permitting transient simulation. The high-resolution simulations are each integrated for six years

167   with the first year ignored as a true spin-up, leaving five years of data for each time period. The high-

168   resolution grid is, in truth, a regionally refined mesh in which a 25 km global resolution is refined to

169   approximately 2.5 km, following Danilov (2022), primarily south of 40 °S, but with other pertinent

170   regions, such as the Agulhas Current and several narrow straits, also refined. In this way, the model is

171   able to simultaneously achieve eddy-rich conditions in the Southern Ocean and many of the nearby active

172   regions, as well as a global resolution that would still be considered high in the context of CMIP6

173   (Hallberg, 2013; Hewitt et al., 2020). While model drift may be a concern with such a short true spin-up

174   period, this should affect each of the high-resolution time slices similarly and to a limited extent due to

175   their short integration lengths. Thus, the differences between the high-resolution ocean simulations should

176   primarily reflect anthropogenic climate impacts simulated during the eddy-permitting transient run and

177   present in the forcing dataset.

178   **2.2 Model configuration**

179   The Finite volume Sea-ice Ocean Model version 2.5 is a post-CMIP6 era model, having been

180   refactored to a finite-volume configuration from the finite-element version (FESOM1.4, Q. Wang et al.,

181   2014) employed in CMIP6, and transitioned to arbitrary Lagrangian Eulerian vertical coordinates, among

182   other improvements (Danilov et al., 2017; Scholz et al., 2019, 2021). FESOM's most distinguishing

183   feature among mature ocean models is the unstructured horizontal grid that exploits triangular grid cells

184   which can smoothly vary in size to change the horizontal grid resolution in space. In these simulations,

185   full free surface, or z*, vertical coordinates were used, allowing the vertical model layer thicknesses to

186   change in time. Gent-McWilliams eddy parameterization (Gent and McWilliams, 1990) is scaled with

187   resolution according to Ferrari et al. (2010) and vertical mixing is simulated by a *k*-profile

188   parameterization scheme (Large et al., 1994).

189   The SO3 mesh consists of over 22 million surface elements (triangle faces) or 11 million surface

190   nodes (triangle vertices) and 70 vertical layers. The simulations produce about 1.1 terabytes of data per

191   year of 3D data stored on nodes. For reference, the medium-resolution mesh used in the AWI-CM-1

192   ensemble is 1.6 million surface elements or 0.83 million surface nodes and 46 vertical layers and

193   produces approximately 56 GB per year of 3D data stored on nodes. The model was run on 8192 CPU

194   cores and with a typical throughput of approximately 0.65 simulated years per day, consuming

195   approximately 5.5 million CPU hours in total despite the various cost-saving modeling approaches. It

196   should be noted, however, that the throughput in high-resolution production simulations like this is highly

197   dependent on the volume and choice of data being saved. The simulations and following analysis were

198   performed using the high-performance computing system, Levante, at the German Climate Computing

199   Center (DKRZ).

200   The ocean model is forced by several atmospheric variables at a six-hour resolution, although one

201   forcing variable, humidity, is interpolated monthly data. The forcing data is supplied to the model on the

202   regular atmospheric grid used in the coupled setup during AWI-CM-1-1-MR's CMIP6 simulations

203   (Semmler et al., 2018) and interpolated to the multi-resolution grid used in the respective simulations by

204   FESOM. Runoff data is a monthly climatology and dynamic ice sheet coupling is not included, meaning

205   the freshwater influx from the Antarctic continent does not react to warming which may impact certain

206   processes, such as the timing and intensity of sea ice loss (Pauling et al., 2017; Bronselaer et al., 2018).

207   **2.3 Modeled ocean velocity data**

208   Geostrophic balance is an idealized approximation that does not match real ocean velocities for

209   several reasons, including the presence of ageostrophic flow, such as Ekman transport, as well as

210 assumptions made in the derivation of equations (1) and (2). Specifically, geostrophic balance between

211 the Coriolis effect and the pressure gradient is valid under the assumption that the curl of horizontal

212 velocities or vorticity is small relative to the magnitude of overall flow. In models, this assumption is

213 relatively close to reality in coarse-resolution simulations where geostrophic flow dominates, but on

214 higher-resolution meshes, where submesoscale flows are well-resolved, these omitted terms become

215 larger. Therefore, while using geostrophic velocities for both high-resolution and coarse-resolution

216 modeled datasets would be methodologically consistent, the error introduced would be systemically larger

217 for the finer-resolution dataset than the coarser. Therefore, we do not consider the use of geostrophic

218 velocities for both modeled datasets in this analysis to bring the data into closer agreement. Rather, for the

219 AWI-CM-1 dataset, where daily ocean velocities were not saved (Semmler et al., 2018), geostrophic

220 velocities derived from sea surface height with equations (1) and (2) are the best possible choice, and

221 fortunately, as described earlier, the error introduced by the assumptions of geostrophic balance will be

222 small. For the SO3 simulations, direct model output was saved and is preferred, particularly given the

223 high resolution of the mesh.

224 $u = -g/f * \partial SSH/\partial y$ (1)

225 $v = g/f * \partial SSH/\partial x$ (2)

226 The omission of Ekman transport, the primary source of ageostrophic oceanic flow from atmospheric

227 influences, can be relatively well addressed in the SO3 dataset by selecting modeled velocities just below

228 the Ekman layer. At depths of 25-30m below sea level, the bulk of Ekman transport can be avoided (Price

229 et al., 1987), while velocities should not substantially differ from those at the surface. What ageostrophic

230 flow remains in the model output velocities should be primarily large-scale and small relative to

231 geostrophic flow in the high-energy regions of the ocean, including the ACC (Yu et al., 2021).

232 **2.4 Altimetry data**

233   An observational data product of gridded, daily geostrophic velocities derived from along-track

234   satellite altimetry from crossover data is taken from the Data Unification and Altimeter Combination

235   System (DUACS) (Taburet et al., 2019). The gridded product has a resolution of 0.25 °, although

236   effective resolution at high latitudes may be much lower (Ballarotta et al., 2019). Recently, improved data

237   has become available in the ice-covered regions of the Southern Ocean (Auger et al., 2022), but does not

238   yet cover the full present-day simulated period (2016-2020) in this study. Absolute velocities from the

239   gridded altimetry product were used to calculate anomalies and EKE using equations (3) and (4) below

240   for consistency with the modeled dataset.

241   **2.5 EKE analysis**

242   Velocity anomalies are defined by subtracting the multi-year monthly climatology of each

243   respective 5-year period from daily velocities with equation (3).

244    $u'_i = u_i - \overline{u_m}$ (3)

245   Where u_i is the daily zonal velocity, $'$ denotes an anomaly, and $\overline{u_m}$ is a monthly mean. For meridional

246   velocities (v) substitute u with v.

247   Eddy kinetic energy is calculated from ocean velocities according to equation (4).

248    $EKE_i = 0.5(u'^2_i + v'^2_i)$ (4)

249   Where ($_i$) denotes a daily value and ($'$) denotes an anomaly.

250   EKE was calculated on the native grid of each dataset and then interpolated to a 0.25 ° grid for all

251   analyses. In Fig. 1 and 3, EKE was first calculated on a daily timescale and coarsened to five-day means

252   before analysis to reduce computational costs during post-processing. Area-integrated EKE (Figure 1, 3)

253   is calculated by summing the area-weighted EKE of each grid cell in the study region defined as the zonal

254   band between 45 °S and 65 °S. The Brazil/Malvinas confluence region between 57 °E and 29 °E and

255   northward of 40 °S is removed to focus the study on a region with consistent physical drivers theorized to

256   be responsible for the changes in eddy activity (Beech et al., 2022). As a precaution, Each dataset was

257   linearly detrended before analysis in Fig. 1 and 3 to avoid artificially increasing the range of the later

258   distributions due to the accelerating climate change signal. Select statistical properties are reported in

259   Supplementary Tables 1-3 to indicate deviations from normality (D'Agostino and Belanger, 1990; Fisher,

260   1997) and autocorrelation (Durbin and Watson, 1950). Rather than attempt to manipulate the data to meet

261   certain statistical assumptions, complex statistical tests are avoided and the statistical properties reported

262   can be used to interpret the EKE data in a physical sense. EKE anomalies (Figure 1) were calculated by

263   subtracting the 2016-2020 mean of area-integrated EKE from the 5-day mean values of each period.

264   Normalized EKE was calculated by further dividing EKE anomaly by the standard deviation of EKE

265   during the 2016-2020 period. In Fig. 4, ensemble agreement is determined by ordering the ΔEKE values

266   within each grid cell from lowest to highest, plotting the positive values in increasing order from left to

267   right and negative values in decreasing order from left to right.

268   **3   Results**

269   **3.1 Agreement with observations**

270   During the five-year period of overlap with observations, the SO3 simulation is a drastic

271   improvement on the AWI-CM-1 ensemble in reproducing median observed EKE (Figure 1a, c, note the

272   different y axes); only a slight underrepresentation of EKE remains in the SO3 simulation, although the

273   simulated distribution is somewhat distinct from observations. In comparison, the AWI-CM-1 ensemble,

274   being effectively eddy-permitting in the Southern Ocean, underrepresents observations by approximately

275   55% (Figure 1a, c, note the different y-axis). EKE in SO3 appears more variable than the observations

276   considering its larger range, (Figure 1c, e), and in general, the modeled datasets display greater deviations

277   from a normal distribution than the observations (Figure 1a, b, c; Supplementary Table 2). Nonetheless,

278   relative to the AWI-CM-1 model bias and the magnitude of EKE resolved, the ensemble spread within the

279   AWI-CM-1 dataset is small (Figure 3), suggesting that a single ensemble member of five years duration is

280   sufficient to assess how well a model captures the magnitude of overall Southern Ocean EKE (Figure 1c).

281
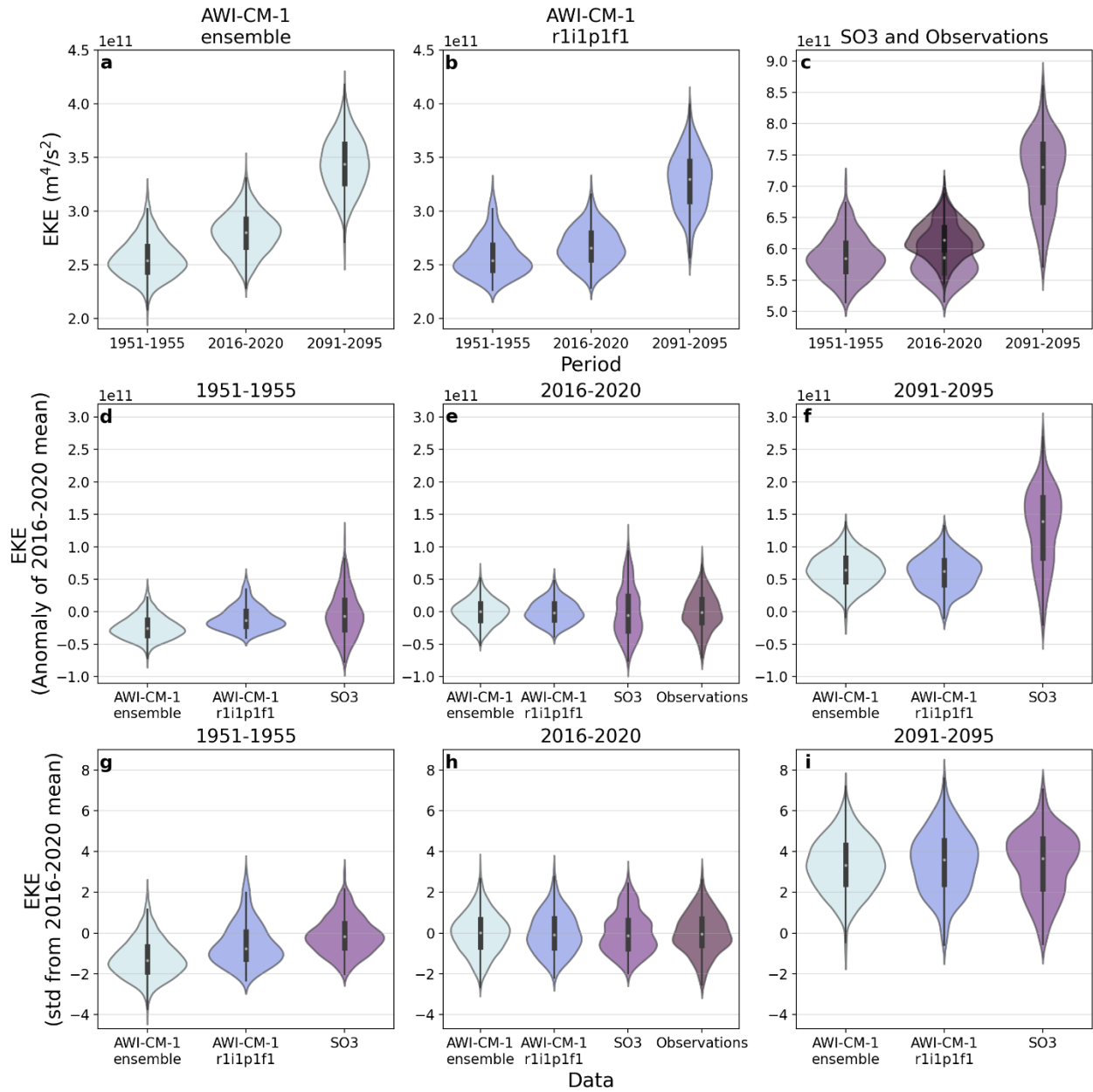
Figure 1. Violin plots of area-integrated Southern Ocean EKE in simulations and observations.
Central points of each plot indicate the median, thick bars span the first and third quartiles, thin bars span
the range, and the violin body is a kernel density estimation of the data. **a-c)** Magnitudes of area-
integrated EKE (note the different y axes) **a)** The AWI-CM-1 ensemble. **b)** the first member of the AWI-
CM-1 ensemble, from which the SO3 simulations take their atmospheric forcing. **c)** The SO3 simulations
and observations. **d-f)** Anomalies relative to the 2016-2020 mean of area-integrated EKE for each dataset

288   respectively. **d)** 1951-1955. **e)** 2016-2020. **f)** 2091-2095. **g-i)** Normalized values relative to the mean and

289   standard deviation of EKE during the 2016-2020 period for each dataset respectively. **g)** 1951-1955. **h)**

290   2016-2020. **i)** 2091-2095.

291   From a regional perspective, the SO3 simulation accurately reflects local magnitudes of observed

292   EKE and also generally captures the spatial distribution well (Figure 2). However, there are regional

293   shortcomings, such as between 90 and 145 °E. Grid resolution in this region should be sufficient to

294   resolve eddy activity (Supplementary Figure 1), indicating that the bias arises from another source. In the

295   AWI-CM-1 ensemble, the regional representation of EKE reinforces a broad underrepresentation relative

296   to observed magnitudes, but the major geographic features of eddy activity are fairly well represented

297   (Figure 2). Once again, the ensemble spread within the AWI-CM-1 simulations reveals remarkable

298   consistency, this time in terms of the spatial pattern and regional magnitudes (Supplementary Figure 2),

299   reinforcing the conclusion that a single ensemble member of five years duration is sufficient to assess the

300   mean state of EKE in the Southern Ocean. The consistency of the AWI-CM-1 ensemble further suggests

301   that regional shortcomings in eddy activity in the SO3 simulations are not a product of variability within a

302   single realization of Southern Ocean conditions (Supplementary Figure 2).
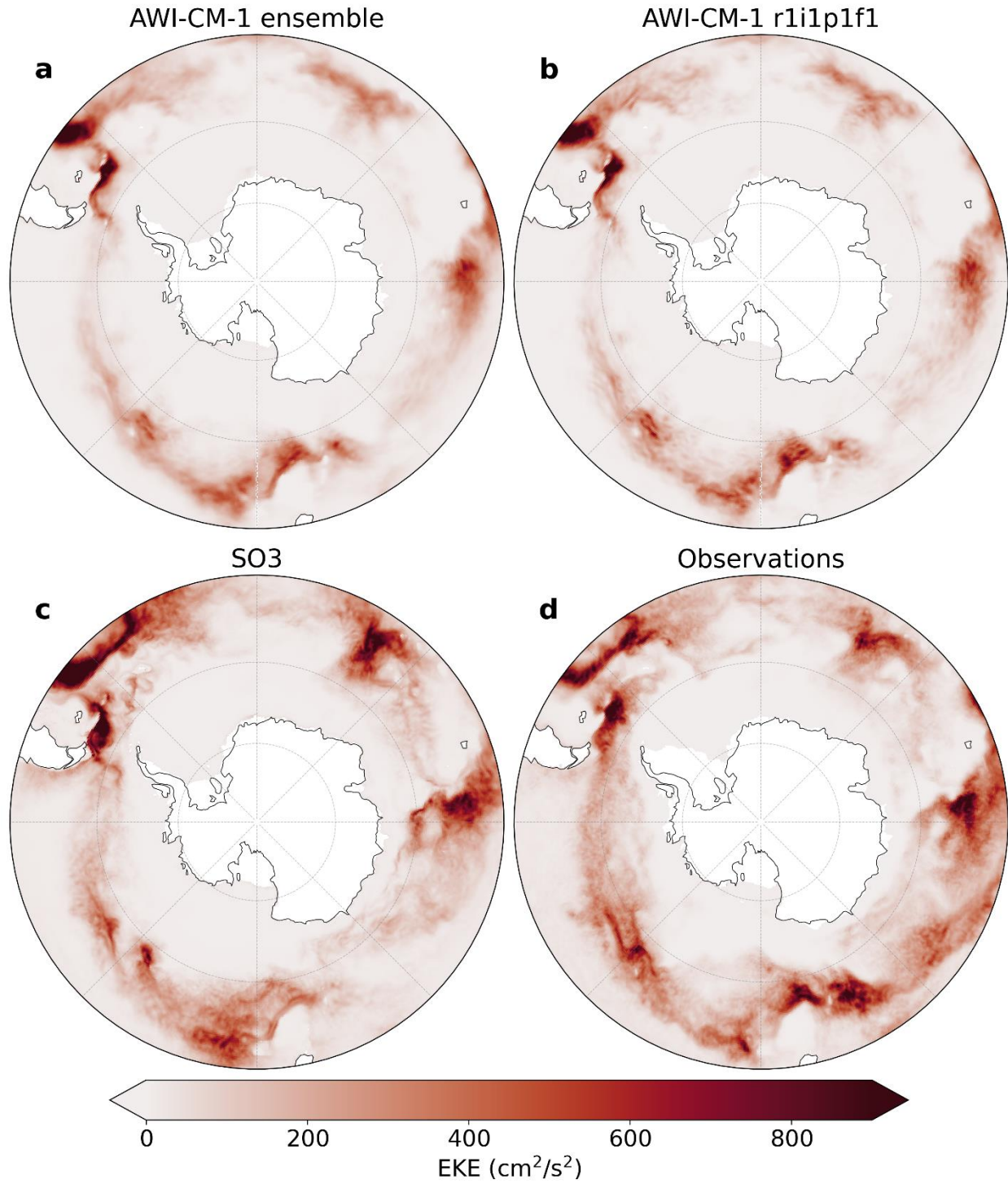
Figure 2. Mean eddy kinetic energy between 2016 and 2020. a) The AWI-CM-1 ensemble. **b)** The first member of the AWI-CM-1 ensemble. **c)** The SO3 simulation. **d)** The gridded satellite altimetry dataset.

3.2 EKE change and significance

308   Southern Ocean eddy activity has been shown to intensify over the recent decades both using

309   satellite altimetry (Martínez-Moreno et al., 2021), and the complete AWI-CM-1-1 dataset from CMIP6

310   (Beech et al., 2022). Even after reducing the AWI-CM-1 CMIP6 dataset to five-year periods preceding

311   the apparent change (1951-1955) and at the end of the altimetry era (2016-2020), this intensification is

312   still discernable within the AWI-CM-1 ensemble (Figure 1a). Despite this, the SO3 simulations do not

313   demonstrate any substantial change in EKE magnitude over the same period (Figure 1). Further reducing

314   the ensemble to its individual members (Figure 3), the EKE rise is still relatively robust in each case,

315   including clear separation of the datasets considering the median, mode, and distribution of the data.

316   However, the first ensemble member, from which the atmospheric forcing of SO3 is taken, demonstrates

317   less EKE rise than the ensemble average (Figure 3), suggesting that natural variability in atmospheric

318   conditions may contribute to the disagreement. Further investigation reveals several differences between

319   the SO3 simulations and the AWI-CM-1 ensemble members that may play a role. Mean zonal ocean

320   velocity in SO3 is faster and broader than the AWI-CM-1 ensemble (Supplementary Figure 3), meaning

321   wind speed intensification may be misaligned with peak ocean velocities in SO3, particularly around 47

322   to 51 °S. Moreover, considerably less zonal wind stress is imparted to the ocean in SO3 despite identical

323   wind speeds as the first AWI-CM-1 ensemble member (Supplementary Figure 4), possibly due to the

324   higher ocean surface velocity.

325   The intensification of EKE becomes clear in both the AWI-CM-1 ensemble (Figure 1a), its

326   members (Figure 3), and the SO3 simulations (Figure 1c) by the end of the 21st century. Over this period,

327   the variability of EKE, indicated by the range of the distribution, also increases for each dataset (Figure

328   1f, i). EKE rise in SO3 is approximately twice that of the AWI-CM1 ensemble in absolute terms (Figure

329   1f), but expressing EKE as a relative value normalized by the mean and standard deviation of each dataset

330   during the observational period (Figure 1g, h, i), reveals greater consistency between the changes until the

331   end of the 21st century. EKE in each dataset appears to increase by approximately 3.5 standard deviations,

and the range of EKE distributions increases by approximately two to three standard deviations (Figure

1h, i). However, the datasets also tend to become more autocorrelated, which can inflate the distribution

range (Supplementary Tables 1, 3).
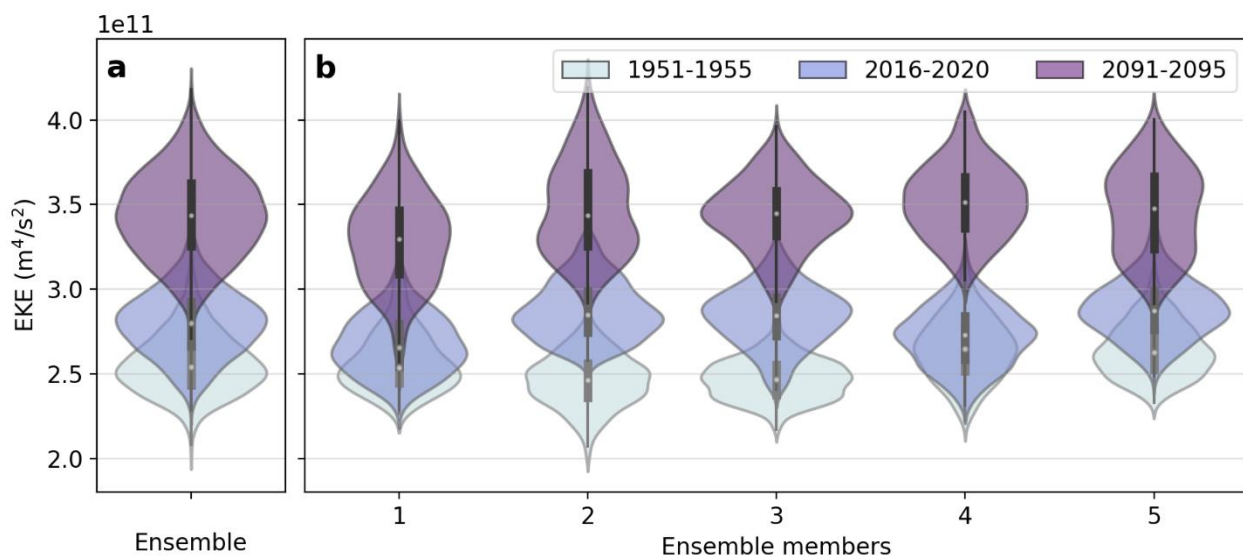
**Figure 3. Ensemble spread of EKE in AWI-CM-1. a)** Violin plots of area-integrated Southern Ocean

EKE in the AWI-CM-1 ensemble. **b)** Violin plots of mean Southern Ocean EKE in each member of the

AWI-CM-1 ensemble. Grey plots represent the period 1951-1955, blue plots represent 2016-2020, and

purple plots represent 2091-2095.

Before considering the regional impacts of warming on EKE in the SO3 simulations, it is useful

to refer to the ensemble spread within the AWI-CM-1 simulations to approximate the reliability of a

single ensemble member in revealing the ensemble-mean change as an analogue to the signal-to-noise

ratio. At 1 °C of warming, EKE change in the ensemble is weak, with at least one ensemble member

tending to show little or no EKE change in most regions (Figure 4a,c). Only a few clear patterns of

change emerge throughout the ensemble, namely the regions of EKE intensification downstream of the

Kerguelen Plateau and the Campbell Plateau where four to five out of five ensemble members show clear

EKE intensification (Figure 4a). It should be noted that even in these regions of relatively high confidence

349   (4 to 5 ensemble members, Figure 4a) EKE rise can be interspersed with lower-confidence (1 to 2

350   ensemble members, Figure 4c) EKE decline; this is also illustrated by the ensemble mean changes

351   themselves (Supplementary Figures 5, 6). Despite this, the consistency of EKE rise in these regions, and

352   their geographic positions in already EKE-rich regions, suggests that the intensification patterns are

353   robust changes within substantial noise. This level of noise suggests that EKE changes in the SO3

354   simulations at 1 °C of warming will be difficult to distinguish from natural variability when taken on their

355   own; indeed, in the SO3 simulations, the large variability of both sign and magnitude of change within

356   relatively small spatial scales does not lend confidence to any significant change at 1 °C of warming

357   (Figure 5c). However, building on the changes observed in the AWI-CM-1 ensemble, the intensification

358   of EKE downstream of the Kerguelen and Campbell Plateaus seems to be reinforced by the high-

359   resolution simulations.
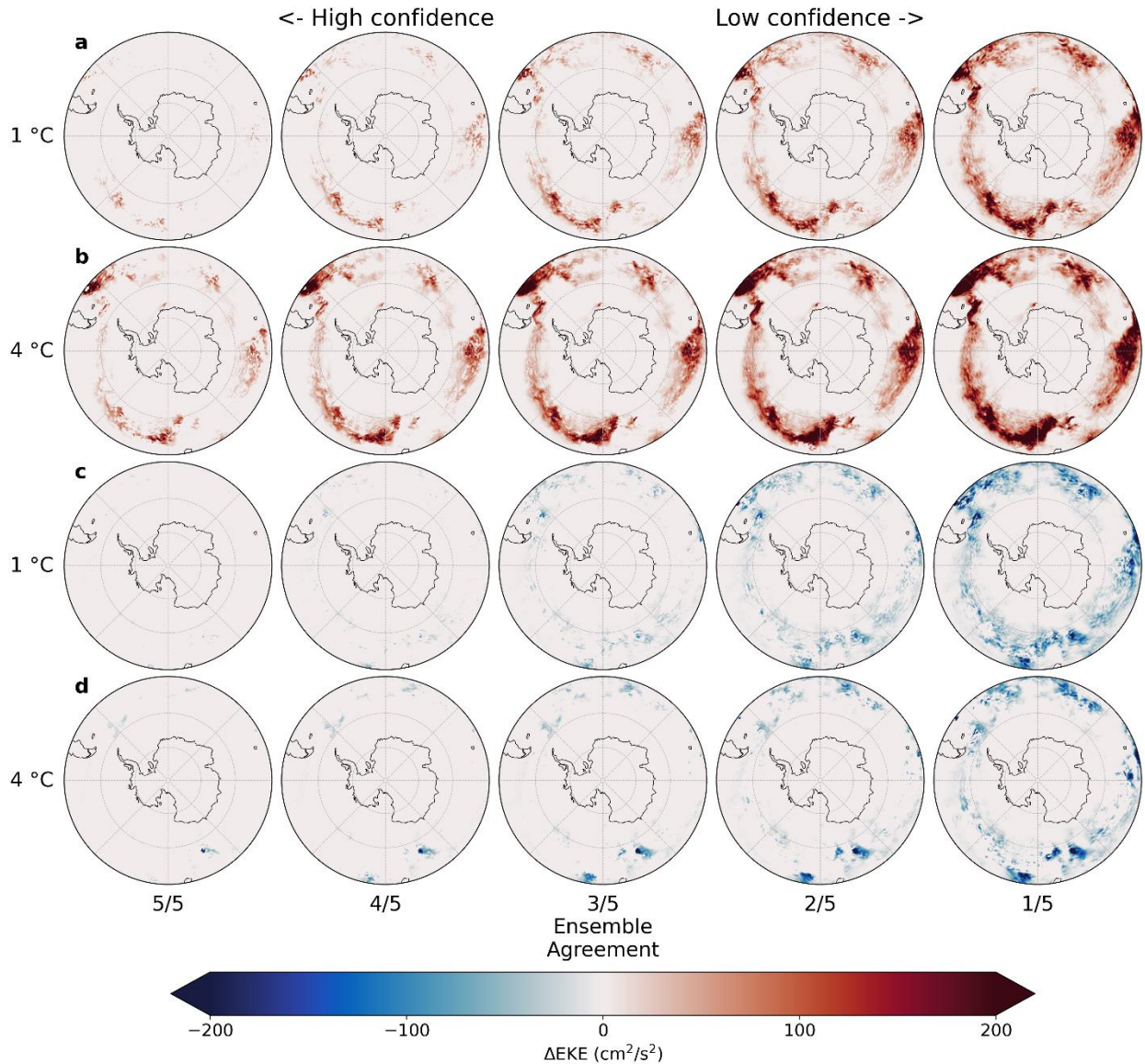
Figure 4. Ensemble agreement regarding EKE change. EKE rise (a, b) and decline (c, d) within the

AWI-CM-1 ensemble after one (a, c) and four (b, d) °C of warming or between 1951-1955 and 2016-

2020 and 2091-2095, respectively, arranged in order of decreasing ensemble agreement regarding change

in each grid cell. Ensemble agreement refers to the number of ensemble members that simulate at least the

pictured magnitude of mean EKE rise or decline for each grid cell. Mean EKE change is defined as the

difference of mean EKE between 1951-1955 and each of the two latter periods, as in Supplementary

Figures 5 and 6 but arranged in ascending order of magnitude for each grid cell and for positive and

negative signs separately. Rank 5/5 indicates the lowest magnitude of mean EKE rise (a, b) or decline (c,

369   d) within the ensemble for a given grid cell, meaning the entire ensemble agrees on at least this much

370   change. Rank 1/5 indicates the highest magnitude of EKE rise or decline within the ensemble for each

371   grid cell, representing the upper limit of projected EKE change.

372   At 4 °C of warming, change in eddy activity becomes clearer; EKE intensification downstream of

373   the Kerguelen and Campbell Plateaus is now consistent throughout the entire AWI-CM-1 ensemble, along

374   with additional intensifications south of the Falkland/Malvinas Plateau, around the Conrad Rise, and

375   along the Antarctic Slope Current at approximately 5 °E (Figure 4b). Four fifths of the ensemble also

376   include a broad increase in EKE throughout the ACC across most longitudes. Interestingly, a consistent

377   pattern of EKE decline also emerges upstream of the Campbell Plateau in the entire ensemble (Figure 4d).

378   The spatial pattern of EKE rise is relatively consistent regardless of confidence, with only the magnitude

379   increasing in the lower confidence composites (Figure 4b). The same tendency is observable between the

380   EKE changes at 1 and 4 °C of warming, where the magnitude of change is greater after further warming

381   but follows the same spatial pattern. Thus, regions of intensification can be identified more reliably than

382   the magnitude of change and tend to be concentrated where flow interacts with topographic features, in

383   already eddy-rich regions (Figure 2). Conversely, low confidence EKE decline appears nearly throughout

384   the Southern Ocean in at least one ensemble member, but only consistently upstream of the Campbell

385   Plateau and, to a far lesser extent, downstream of the Drake Passage and Campbell Plateau (Figure 4d).

386   Changes of negative sign tend to be of lower magnitude at 4 °C of warming than at 1 °C. This suggests

387   that the general EKE response to climate change in the Southern Ocean is that of intensification, and the

388   interspersed signals of decline tend to be the result of natural variability. Yet, small regions of high-

389   confidence EKE decline also appear. Consequently, it would be difficult to confidently separate reliable

390   EKE change from natural variability in simulations without an ensemble to compare with. In the SO3

391   simulations, EKE rise downstream of the Drake Passage and Kerguelen and Campbell Plateaus is

392   substantial (Figure 5f). EKE rise is also projected south of the Falkland/Malvinas Plateau, around the

393   Conrad Rise, and along the Antarctic Slope Current at approximately 5 °E, and a slight EKE decline

appears upstream of the Campbell Plateau. All of this is comparable to the AWI-CM-1 ensemble, and the

interspersed areas of EKE decline within these regions, for example, around the Conrad Rise, are not

improbable based on the example set by AWI-CM-1 (Figure 4d). However, considering that some high-

confidence EKE decline is present in the AWI-CM-1 ensemble, it is difficult to confidently dismiss

regional EKE decline in the SO3 simulations as noise.
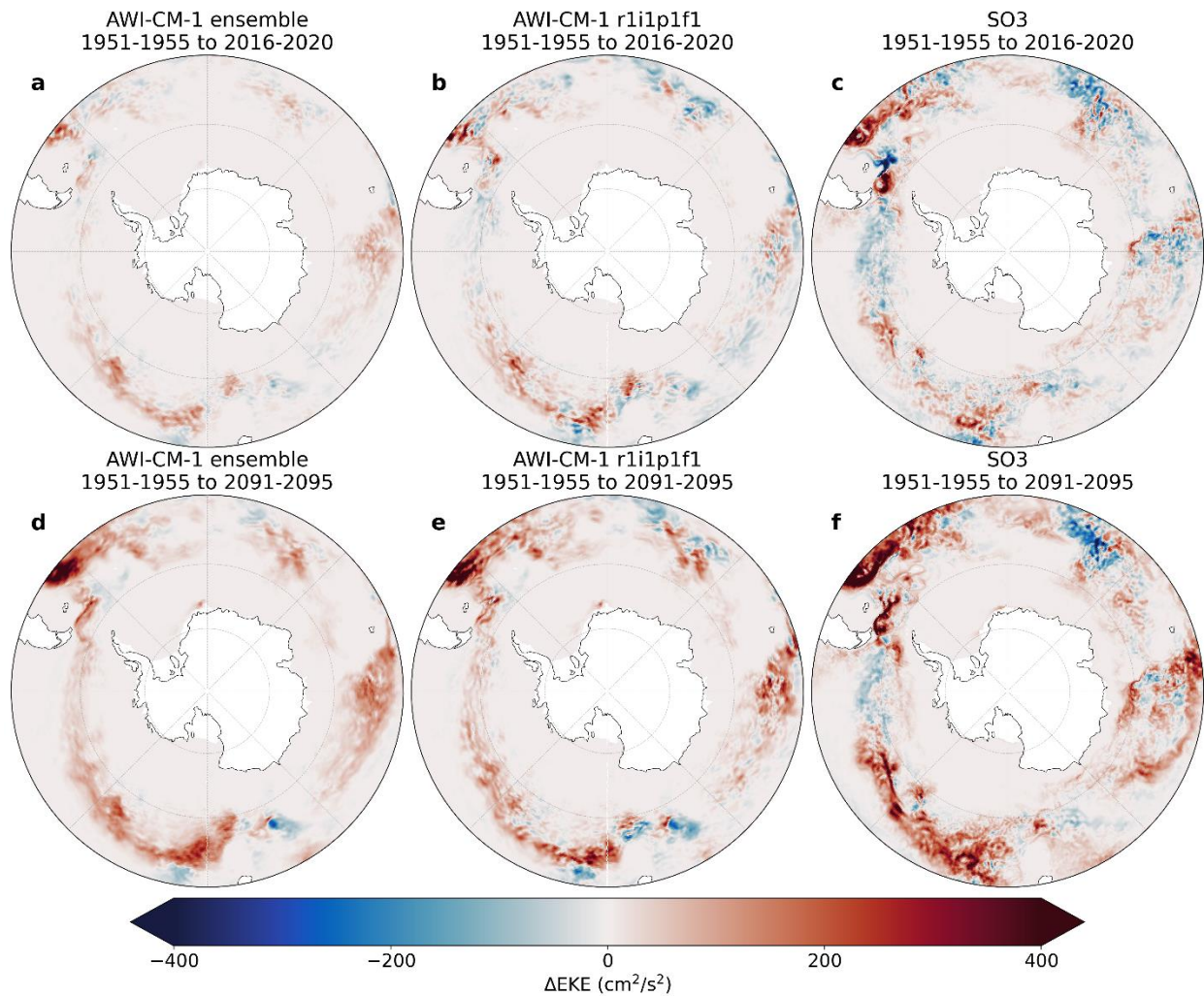
Figure 5. EKE change. Spatial representations of the difference in EKE between **(a-c)** 1951-1955 and

2016-2020, **(d-f)** 1951-1955 and 2091-2095. **a,d)** The AWI-CM-1 ensemble. **b,e)** the first member of the

AWI-CM-1 ensemble. **c,f)** The SO3 simulations.

4 Discussion

Intensification of eddy activity in the Southern Ocean is now widely accepted as a consequence of anthropogenic climate change (Hogg et al., 2015; Patara et al., 2016; Martínez-Moreno et al., 2021; Beech et al., 2022), and is understood to be caused primarily by stronger westerly winds imparting more energy to the Antarctic Circumpolar Current (Munday et al., 2013; Marshall, 2003). The results presented here reinforce the notion of EKE intensification and further project increased EKE variability as the climate warms (Figure 1, 3). By expressing EKE change in terms of ensemble agreement on a cell-by-cell basis, the results presented here are also able to identify regions of reliable and substantial change as those where flow interacts with major bathymetric features and high eddy activity is already known to occur (Figure 4). Analysis of regional changes within the Southern Ocean eddy field has generally been limited to regions defined by oceanic sectors (Atlantic, Indian, Pacific) (Hogg et al., 2015), or incremental longitudinal delimitations (Patara et al., 2016). In future research, regional analyses of the significance, rate, or cause of EKE trends could focus on the bathymetrically defined regions identified in this analysis to produce physically related and consistent results.

The consistency of the AWI-CM-1 ensemble in projecting clear EKE rise in the Southern Ocean as a whole suggests that a single ensemble member of five-years simulation length should be sufficient to reliably identify change, even after 1 °C of temperature rise. Despite this, the SO3 simulations fail to reproduce the EKE rise that is already observable through observations (Martínez-Moreno et al., 2021). A potential source for this discrepancy is the uncoupled model setup in the SO3 simulations which omits ocean-atmosphere feedbacks. In this regard, the SO3 simulations experience lower wind stress imparted to the ocean surface than AWI-CM-1 ensemble member one by the same surface winds (Supplementary Figure 4), and a mismatch between peak zonal wind speeds and mean zonal ocean velocities (Supplementary Figure 3). Confounding the comparison further, is the fact that strengthening winds can both increase and dampen eddy activity; as westerlies intensify, the additional energy imparted to the ocean is expected to strengthen eddy activity (Munday et al., 2013; Meredith and Hogg, 2006), but winds

429   are also known to dampen mesoscale activity through eddy killing (Rai et al., 2021) and this impact is

430   greater in uncoupled model configurations (Renault et al., 2016). While the lack of change at 1 °C is

431   difficult to explain, the disagreement is limited to these more subtle changes and the simulations tend to

432   agree on the strong EKE rise at 4 °C of warming.

433   The remaining discrepancies between eddy activity in SO3 and observations are relatively small,

434   but exploring potential sources of disagreement may help to interpret the simulations and guide future

435   modeling endeavors. Greater skew in the distribution of EKE in the modeled dataset (Supplementary

436   Table 2) could reflect multiple modes of circulation or seasonality. While seasonality of eddy activity in

437   the ACC is low, seasonal ice cover likely affects eddy activity in the modeled dataset, and certainly

438   affects the observational dataset by producing gaps in its spatio-temporal coverage. Beyond differences in

439   skew, this could contribute to the greater range of EKE seen in the SO3 simulations by systemically

440   obscuring seasonal conditions from the observational dataset. Regional deficiencies of EKE in SO3 could

441   be explained in terms of grid resolution outside of the study region; resolving the first Rossby radius of

442   deformation with at least two grid points is not enough to comprehensively reproduce mesoscale activity

443   (Hallberg, 2013; Sein et al., 2017), and grid refinement may need to be expanded to upstream regions that

444   impact eddy dynamics in the Southern Ocean. Other sources of bias may include ocean-atmosphere

445   interactions which are absent or unrealistic within the uncoupled simulations (Byrne et al., 2016; Rai et

446   al., 2021; Renault et al., 2016). As well, some small-scale, slow-to-equilibrate ocean processes may be

447   resolved in the high-resolution simulations, but not be integrated long enough for their effects to impact

448   eddy activity (van Westen and Dijkstra, 2021; Rackow et al., 2022). Finally, the gridded altimetry product

449   itself may be responsible for some disagreement, as the along-track data is known to underrepresent eddy

450   activity at scales less than 150km and 10 days (Chassignet and Xu, 2017), which will be particularly

451   impactful at high latitudes.

452   To distinguish a meaningful signal of anthropogenic impacts from natural variability, this

453   analysis relies primarily on consistency among ensemble members (Figures 3, 4). This is distinct from

454   more traditional methods like assessment of error relative to observations or ensemble mean, commonly

455   applied to weather forecasting (Ferro et al., 2012), but can be compared to measures of ensemble

456   agreement used extensively in the IPCC reports (Fox-Kemper et al., 2021). Performance evaluation

457   relative to observations would undoubtedly point to the high-resolution simulation as superior due to the

458   drastic underrepresentation of EKE in the eddy-permitting ensemble (Figure 1). Yet, the effects of climate

459   change are still apparent in the AWI-CM-1 ensemble (Figure 1, 5), and the AWI-CM-1 dataset has been

460   used to make similar projections of EKE already (Beech et al., 2022). Moreover, the eddy response to

461   forcing seems to be consistent between the model resolutions when expressed in relative (Figure 1g, h, i),

462   rather than absolute terms (Figure 1a, b, c). While more verification of this result is necessary both

463   regionally, and with other models, these results suggest that eddy-permitting resolutions can be

464   interpreted with their shortcomings in mind in order to discern the real-world implications: as is often

465   necessary with model data. Thus, based on the test case of the Southern Ocean, the usefulness of the

466   AWI-CM-1 ensemble and the effectiveness of model simulations in identifying physically significant and

467   reproduceable impacts of climate change may be greater than would be identified using traditional

468   methods and comes at a much lower cost relative to the eddy-resolving simulations.

469   This study has focused on EKE as an evaluation metric for the simulations since mesoscale

470   activity is the primary motivation for increasing ocean model resolution. It has stopped short of assessing

471   the improvements that resolving the mesoscale has on climate and ocean dynamics, many of which are

472   discussed in detail elsewhere (eg. Hewitt et al., 2017). Rather than repeat an assessment of the benefits of

473   resolving smaller scales, we assume that the accurate reproduction and evolution of eddy activity

474   indicates that these improvements are transferred to broader processes. Certainly, inaccurate simulation of

475   the mesoscale would raise questions regarding the improvements that this mesoscale activity should have

476   on the simulations as a whole. Nonetheless, further evaluation of the modeling approaches employed in

477   this study will be necessary to determine if these methods are appropriate for studying broader elements

478   of the climate system. Since the high-resolution simulations derive their deep-ocean climate primarily

479   from the medium-resolution spin-up simulation, improving the initialization process (Thiria et al., 2023)

480   may be the critical barrier to extending these results from the mixed layer to the deeper ocean.

481   **5 Conclusion**

482   Resolving the ocean mesoscale has become a focus for the climate and ocean modeling

483   community as computational capabilities expand and models become increasingly complex. The benefits

484   that explicitly resolved eddy activity can have on climate simulations are clear (Hewitt et al., 2017; Sein

485   et al., 2017) along with the impact that mesoscale variability has on local (Lachkar et al., 2009; Wang et

486   al., 2017) and global environments (Falkowski et al., 1991; Sallée et al., 2012). However, state-of-the-art

487   climate models will be unable to fully resolve the mesoscale for the foreseeable future, particularly in

488   large-scale modeling endeavors such as CMIP (Hewitt et al., 2020). Thus, modelers must make informed

489   choices regarding the explicit processes needed to answer research questions and where resources must be

490   allocated to achieve specific goals. Existing analysis of resource allocation has typically addressed short-

491   term weather forecasting or the ability to reproduce observations with low error (Ferro et al., 2012), but

492   the question of how to best allocate resources for climate change impact assessment remains. This study

493   has applied several cost-efficient modeling approaches to an analysis of the impacts of climate change on

494   a key focus of high-resolution modeling: the mesoscale. Applying these results to broader climate change

495   impact studies should improve the efficiency of resource allocation and focus modeling studies.

496   Resolution can be dynamically adjusted both spatially, by focusing resources in study regions and where

497   they are necessary to resolve local dynamics, and temporally, by allowing lower-resolution workhorse

498   configurations to perform spin-up and transient runs. Limited simulation length and ensemble size can be

499   sufficient for certain research questions and validation, but simulations must ultimately be designed to

500   meet their specific goals. Where resources are limited, studies may best include a combination of eddy-

501   resolving simulations able to fully capture the local eddy field, as well as eddy-permitting simulations that

502   can attest to the significance of results through consistency and repetition.

503   This work represents a contribution to the growing wealth of research that points to an

504   intensification of eddy activity in the Southern Ocean (Hogg et al., 2015; Martínez-Moreno et al., 2021;

505   Beech et al., 2022). The further conclusions that EKE variability may increase and that EKE

506   intensification appears concentrated in key regions based on topography can both expand the present state

507   of knowledge, as well as direct future research. The cost-efficient modeling approaches of regional grid

508   refinement, reduced-resolution spin-up and transient runs, and limited simulation lengths distinguished by

509   longer periods of change are demonstrated to be effective at reproducing change within a more traditional

510   eddy-permitting ensemble. When resources are limited and resolution demands are high, these approaches

511   can be adapted to address specific research questions. Where assessing the robustness of change is

512   critical, the complimentary eddy-permitting ensemble represents an effective, low-cost supplement to the

513   high-resolution simulations.

514

515

516

Data Availability

517

518   Geostrophic velocities derived from satellite altimetry data are publicly available at

519 https://doi.org/10.48670/moi-00148. Daily sea surface height data from AWI-CM-1-1-MR in CMIP6

520 used to compute geostrophic velocities in this study is archived at the World Data Center for Climate at

521 the DKRZ (https://doi.org/10.26050/WDCC/C6sCMAWAWM,

522 https://doi.org/10.26050/WDCC/C6sSPAWAWM) (Semmler et al., 2022a, b). Model output from AWI-

523 CM-1-1-MR in the CMIP6 framework, including all variables used to force the standalone ocean

524 simulations conducted for this study, is publicly available at https://doi.org/10.22033/ESGF/CMIP6.359

525 (Semmler et al., 2018). Eddy kinetic energy datasets calculated from FESOM output velocities are

526 available at https://doi.org/10.5281/zenodo.8046792 (Beech, 2023b).

Code Availability

527

528   Source code for the ocean model FESOM2 is available at (https:/doi.org/

529 10.5281/zenodo.7737061) (patrickscholz et al., 2023). Code used for data analysis and visualization in

530 this study is publicly available at (https://doi.org/10.5281/zenodo.8046782) (Beech, 2023a). Code used

531 to calculate geostrophic velocities from sea surface height data from AWI-CM-1-1-MR is available from

532 https://doi.org/10.5281/zenodo.7050573.

Author Contributions

533

534 NB, TJ, TR, and TS conceived of the study. NB carried out the simulations, analyzed the data, and drafted

535 the manuscript. All authors reviewed the manuscript.

Competing Interests

536

537 The authors declare no competing interests.

Acknowledgements

538

549

550

References

Auger, M., Prandi, P., and Sallée, J.-B.: Southern ocean sea level anomaly in the sea ice-covered sector from multimission satellite observations, Sci. Data, 9, 70, https://doi.org/10.1038/s41597-022-01166-z, 2022.

Auger, M., Sallée, J.-B., Thompson, A. F., Pauthenet, E., and Prandi, P.: Southern Ocean Ice-Covered Eddy Properties From Satellite Altimetry, J. Geophys. Res. Oceans, 128, e2022JC019363, https://doi.org/10.1029/2022JC019363, 2023.

Ballarotta, M., Ubelmann, C., Pujol, M.-I., Taburet, G., Fournier, F., Legeais, J.-F., Faugère, Y., Delepoulle, A., Chelton, D., Dibarboure, G., and Picot, N.: On the resolutions of ocean altimetry maps, Ocean Sci., 15, 1091–1109, https://doi.org/10.5194/os-15-1091-2019, 2019.

Beech, N.: n-beech/Beech_et_al_cost_efficient_SO: Final, https://doi.org/10.5281/zenodo.10185411, 2023a.

Beech, N.: Processed EKE from FESOM-SO3 (1.0), https://doi.org/10.5281/zenodo.8046792, 2023b.

Beech, N., Rackow, T., Semmler, T., Danilov, S., Wang, Q., and Jung, T.: Long-term evolution of ocean eddy activity in a warming world, Nat. Clim. Change, 12, 910–917, https://doi.org/10.1038/s41558-022-01478-3, 2022.

Bishop, S. P., Gent, P. R., Bryan, F. O., Thompson, A. F., Long, M. C., and Abernathey, R.: Southern Ocean Overturning Compensation in an Eddy-Resolving Climate Simulation, J. Phys. Oceanogr., 46, 1575–1592, https://doi.org/10.1175/JPO-D-15-0177.1, 2016.

Bronselaer, B., Winton, M., Griffies, S. M., Hurlin, W. J., Rodgers, K. B., Sergienko, O. V., Stouffer, R. J., and Russell, J. L.: Change in future climate due to Antarctic meltwater, Nature, 564, 53–58, https://doi.org/10.1038/s41586-018-0712-z, 2018.

Byrne, D., Münnich, M., Frenger, I., and Gruber, N.: Mesoscale atmosphere ocean coupling enhances the transfer of wind energy into the ocean, Nat. Commun., 7, ncomms11867, https://doi.org/10.1038/ncomms11867, 2016.

Chassignet, E. P. and Xu, X.: Impact of Horizontal Resolution (1/12° to 1/50°) on Gulf Stream Separation, Penetration, and Variability, J. Phys. Oceanogr., 47, 1999–2021, https://doi.org/10.1175/JPO-D-17-0031.1, 2017.

D'Agostino, R. B. and Belanger, A.: A Suggestion for Using Powerful and Informative Tests of Normality, Am. Stat., 44, 316–321, https://doi.org/10.2307/2684359, 1990.

Danilov, S.: Ocean modeling on unstructured meshes, Ocean Model., 69, 195–210, https://doi.org/10.1016/j.ocemod.2013.05.005, 2013.

Danilov, S.: On the Resolution of Triangular Meshes, J. Adv. Model. Earth Syst., 14, e2022MS003177, https://doi.org/10.1029/2022MS003177, 2022.

Danilov, S., Sidorenko, D., Wang, Q., and Jung, T.: The Finite-volumE Sea ice–Ocean Model (FESOM2), Geosci. Model Dev., 10, 765–789, https://doi.org/10.5194/gmd-10-765-2017, 2017.

587   Durbin, J. and Watson, G. S.: Testing for Serial Correlation in Least Squares Regression. I, Biometrika, 37,
588   409–428, https://doi.org/10.1093/biomet/37.3-4.409, 1950.

589   Eyring, V., Bony, S., Meehl, G. A., Senior, C. A., Stevens, B., Stouffer, R. J., and Taylor, K. E.: Overview of
590   the Coupled Model Intercomparison Project Phase 6 (CMIP6) experimental design and organization,
591   Geosci. Model Dev., 9, 1937–1958, https://doi.org/10.5194/gmd-9-1937-2016, 2016.

592   Falkowski, P. G., Ziemann, D., Kolber, Z., and Bienfang, P. K.: Role of eddy pumping in enhancing primary
593   production in the ocean, Nature, 352, 55–58, https://doi.org/10.1038/352055a0, 1991.

594   Ferrari, R., Griffies, S. M., Nurser, A. J. G., and Vallis, G. K.: A boundary-value problem for the
595   parameterized mesoscale eddy transport, Ocean Model., 32, 143–156,
596   https://doi.org/10.1016/j.ocemod.2010.01.004, 2010.

597   Ferro, C. A. T., Jupp, T. E., Lambert, F. H., Huntingford, C., and Cox, P. M.: Model complexity versus
598   ensemble size: allocating resources for climate prediction, Philos. Trans. R. Soc. Math. Phys. Eng. Sci.,
599   370, 1087–1099, https://doi.org/10.1098/rsta.2011.0307, 2012.

600   Fisher, R. A.: The moments of the distribution for normal samples of measures of departure from
601   normality, Proc. R. Soc. Lond. Ser. Contain. Pap. Math. Phys. Character, 130, 16–28,
602   https://doi.org/10.1098/rspa.1930.0185, 1997.

603   Frölicher, T. L., Sarmiento, J. L., Paynter, D. J., Dunne, J. P., Krasting, J. P., and Winton, M.: Dominance of
604   the Southern Ocean in Anthropogenic Carbon and Heat Uptake in CMIP5 Models, J. Clim., 28, 862–886,
605   https://doi.org/10.1175/JCLI-D-14-00117.1, 2015.

606   Gent, P. R. and McWilliams, J. C.: Isopycnal Mixing in Ocean Circulation Models, J. Phys. Oceanogr., 20,
607   150–155, https://doi.org/10.1175/1520-0485(1990)020<0150:IMIOCM>2.0.CO;2, 1990.

608   Haarsma, R. J., Roberts, M. J., Vidale, P. L., Senior, C. A., Bellucci, A., Bao, Q., Chang, P., Corti, S., Fučkar,
609   N. S., Guemas, V., von Hardenberg, J., Hazeleger, W., Kodama, C., Koenigk, T., Leung, L. R., Lu, J., Luo, J.-
610   J., Mao, J., Mizielinski, M. S., Mizuta, R., Nobre, P., Satoh, M., Scoccimarro, E., Semmler, T., Small, J., and
611   von Storch, J.-S.: High Resolution Model Intercomparison Project (HighResMIP v1.0) for CMIP6, Geosci.
612   Model Dev., 9, 4185–4208, https://doi.org/10.5194/gmd-9-4185-2016, 2016.

613   Hallberg, R.: Using a resolution function to regulate parameterizations of oceanic mesoscale eddy
614   effects, Ocean Model., 72, 92–103, https://doi.org/10.1016/j.ocemod.2013.08.007, 2013.

615   Hewitt, H. T., Bell, M. J., Chassignet, E. P., Czaja, A., Ferreira, D., Griffies, S. M., Hyder, P., McClean, J. L.,
616   New, A. L., and Roberts, M. J.: Will high-resolution global ocean models benefit coupled predictions on
617   short-range to climate timescales?, Ocean Model., 120, 120–136,
618   https://doi.org/10.1016/j.ocemod.2017.11.002, 2017.

619   Hewitt, H. T., Roberts, M., Mathiot, P., Biastoch, A., Blockley, E., Chassignet, E. P., Fox-Kemper, B., Hyder,
620   P., Marshall, D. P., Popova, E., Treguier, A.-M., Zanna, L., Yool, A., Yu, Y., Beadling, R., Bell, M., Kuhlbrodt,
621   T., Arsouze, T., Bellucci, A., Castruccio, F., Gan, B., Putrasahan, D., Roberts, C. D., Van Roekel, L., and
622   Zhang, Q.: Resolving and Parameterising the Ocean Mesoscale in Earth System Models, Curr. Clim.
623   Change Rep., 6, 137–152, https://doi.org/10.1007/s40641-020-00164-w, 2020.

Hogg, A. McC., Meredith, M. P., Chambers, D. P., Abrahamsen, E. P., Hughes, C. W., and Morrison, A. K.: Recent trends in the Southern Ocean eddy field, J. Geophys. Res. Oceans, 120, 257–267, https://doi.org/10.1002/2014JC010470, 2015.

Irving, D., Hobbs, W., Church, J., and Zika, J.: A Mass and Energy Conservation Analysis of Drift in the CMIP6 Ensemble, J. Clim., 34, 3157–3170, https://doi.org/10.1175/JCLI-D-20-0281.1, 2021.

Jungclaus, J. H., Lorenz, S. J., Schmidt, H., Brovkin, V., Brüggemann, N., Chegini, F., Crüger, T., De-Vrese, P., Gayler, V., Giorgetta, M. A., Gutjahr, O., Haak, H., Hagemann, S., Hanke, M., Ilyina, T., Korn, P., Kröger, J., Linardakis, L., Mehlmann, C., Mikolajewicz, U., Müller, W. A., Nabel, J. E. M. S., Notz, D., Pohlmann, H., Putrasahan, D. A., Raddatz, T., Ramme, L., Redler, R., Reick, C. H., Riddick, T., Sam, T., Schneck, R., Schnur, R., Schupfner, M., von Storch, J.-S., Wachsmann, F., Wieners, K.-H., Ziemen, F., Stevens, B., Marotzke, J., and Claussen, M.: The ICON Earth System Model Version 1.0, J. Adv. Model. Earth Syst., 14, e2021MS002813, https://doi.org/10.1029/2021MS002813, 2022.

Lachkar, Z., Orr, J. C., Dutay, J. C., and Delecluse, P.: On the role of mesoscale eddies in the ventilation of Antarctic intermediate water, Deep-Sea Res. Part Oceanogr. Res. Pap., 56, 909–925, https://doi.org/10.1016/j.dsr.2009.01.013, 2009.

Landschützer, P., Gruber, N., Haumann, F. A., Rödenbeck, C., Bakker, D. C. E., van Heuven, S., Hoppema, M., Metzl, N., Sweeney, C., Takahashi, T., Tilbrook, B., and Wanninkhof, R.: The reinvigoration of the Southern Ocean carbon sink, Science, 349, 1221–1224, https://doi.org/10.1126/science.aab2620, 2015.

Large, W. G., McWilliams, J. C., and Doney, S. C.: Oceanic vertical mixing: A review and a model with a nonlocal boundary layer parameterization, Rev. Geophys., 32, 363–403, https://doi.org/10.1029/94RG01872, 1994.

Marshall, G. J.: Trends in the Southern Annular Mode from Observations and Reanalyses, J. Clim., 16, 4134–4143, https://doi.org/10.1175/1520-0442(2003)016<4134:TITSAM>2.0.CO;2, 2003.

Marshall, J., Jones, H., Karsten, R., and Wardle, R.: Can Eddies Set Ocean Stratification?, J. Phys. Oceanogr., 32, 26–38, https://doi.org/10.1175/1520-0485(2002)032<0026:CESOS>2.0.CO;2, 2002.

Martínez-Moreno, J., Hogg, A. McC., England, M. H., Constantinou, N. C., Kiss, A. E., and Morrison, A. K.: Global changes in oceanic mesoscale currents over the satellite altimetry record, Nat. Clim. Change, 11, 397–403, https://doi.org/10.1038/s41558-021-01006-9, 2021.

Marzocchi, A., Hirschi, J. J.-M., Holliday, N. P., Cunningham, S. A., Blaker, A. T., and Coward, A. C.: The North Atlantic subpolar circulation in an eddy-resolving global ocean model, J. Mar. Syst., 142, 126–143, https://doi.org/10.1016/j.jmarsys.2014.10.007, 2015.

Meredith, M. P. and Hogg, A. M.: Circumpolar response of Southern Ocean eddy activity to a change in the Southern Annular Mode, Geophys. Res. Lett., 33, https://doi.org/10.1029/2006GL026499, 2006.

Munday, D. R., Johnson, H. L., and Marshall, D. P.: Eddy Saturation of Equilibrated Circumpolar Currents, J. Phys. Oceanogr., 43, 507–532, https://doi.org/10.1175/JPO-D-12-095.1, 2013.

O'Neill, B. C., Tebaldi, C., van Vuuren, D. P., Eyring, V., Friedlingstein, P., Hurtt, G., Knutti, R., Kriegler, E., Lamarque, J.-F., Lowe, J., Meehl, G. A., Moss, R., Riahi, K., and Sanderson, B. M.: The Scenario Model

Intercomparison Project (ScenarioMIP) for CMIP6, Geosci. Model Dev., 9, 3461–3482, https://doi.org/10.5194/gmd-9-3461-2016, 2016.

O'Neill, B. C., Kriegler, E., Ebi, K. L., Kemp-Benedict, E., Riahi, K., Rothman, D. S., van Ruijven, B. J., van Vuuren, D. P., Birkmann, J., Kok, K., Levy, M., and Solecki, W.: The roads ahead: Narratives for shared socioeconomic pathways describing world futures in the 21st century, Glob. Environ. Change, 42, 169–180, https://doi.org/10.1016/j.gloenvcha.2015.01.004, 2017.

Patara, L., Böning, C. W., and Biastoch, A.: Variability and trends in Southern Ocean eddy activity in 1/12° ocean model simulations, Geophys. Res. Lett., 43, 4517–4523, https://doi.org/10.1002/2016GL069026, 2016.

patrickscholz, dsidoren, Koldunov, N., Hegewald, J., rakowsk, Streffing, J., Rackow, T., ogurses, helgegoessling, Guibert, D., qiangclimate, cwekerle, Oord, G. van den, jrberlin, Miguel, Gierz, P., and Cheedela, S. K.: FESOM/fesom2: FESOM2.5, , https://doi.org/10.5281/zenodo.7737061, 2023.

Pauling, A. G., Smith, I. J., Langhorne, P. J., and Bitz, C. M.: Time-Dependent Freshwater Input From Ice Shelves: Impacts on Antarctic Sea Ice and the Southern Ocean in an Earth System Model, Geophys. Res. Lett., 44, 10,454-10,461, https://doi.org/10.1002/2017GL075017, 2017.

Price, J. F., Weller, R. A., and Schudlich, R. R.: Wind-Driven Ocean Currents and Ekman Transport, Science, 238, 1534–1538, https://doi.org/10.1126/science.238.4833.1534, 1987.

Rackow, T., Danilov, S., Goessling, H. F., Hellmer, H. H., Sein, D. V., Semmler, T., Sidorenko, D., and Jung, T.: Delayed Antarctic sea-ice decline in high-resolution climate change simulations, Nat. Commun., 13, 637, https://doi.org/10.1038/s41467-022-28259-y, 2022.

Rai, S., Hecht, M., Maltrud, M., and Aluie, H.: Scale of oceanic eddy killing by wind from global satellite observations, Sci. Adv., 7, eabf4920, https://doi.org/10.1126/sciadv.abf4920, 2021.

Renault, L., Molemaker, M. J., McWilliams, J. C., Shchepetkin, A. F., Lemarié, F., Chelton, D., Illig, S., and Hall, A.: Modulation of Wind Work by Oceanic Current Interaction with the Atmosphere, J. Phys. Oceanogr., 46, 1685–1704, https://doi.org/10.1175/JPO-D-15-0232.1, 2016.

Ringler, T., Petersen, M., Higdon, R. L., Jacobsen, D., Jones, P. W., and Maltrud, M.: A multi-resolution approach to global ocean modeling, Ocean Model., 69, 211–232, https://doi.org/10.1016/j.ocemod.2013.04.010, 2013.

Sallée, J.-B., Matear, R. J., Rintoul, S. R., and Lenton, A.: Localized subduction of anthropogenic carbon dioxide in the Southern Hemisphere oceans, Nat. Geosci., 5, 579–584, https://doi.org/10.1038/ngeo1523, 2012.

Scholz, P., Sidorenko, D., Gurses, O., Danilov, S., Koldunov, N., Wang, Q., Sein, D., Smolentseva, M., Rakowsky, N., and Jung, T.: Assessment of the Finite-volumE Sea ice-Ocean Model (FESOM2.0) – Part 1: Description of selected key model elements and comparison to its predecessor version, Geosci. Model Dev., 12, 4875–4899, https://doi.org/10.5194/gmd-12-4875-2019, 2019.

Scholz, P., Sidorenko, D., Danilov, S., Wang, Q., Koldunov, N., Sein, D., and Jung, T.: Assessment of the Finite VolumE Sea Ice Ocean Model (FESOM2.0), Part II: Partial bottom cells, embedded sea ice and

698   vertical mixing library CVMIX, Climate and Earth system modeling, https://doi.org/10.5194/gmd-2021-
699   94, 2021.

700   Sein, D. V., Koldunov, N. V., Danilov, S., Wang, Q., Sidorenko, D., Fast, I., Rackow, T., Cabos, W., and Jung,
701   T.: Ocean Modeling on a Mesh With Resolution Following the Local Rossby Radius, J. Adv. Model. Earth
702   Syst., 9, 2601–2614, https://doi.org/10.1002/2017MS001099, 2017.

703   Semmler, T., Danilov, S., Rackow, T., Sidorenko, D., Barbi, D., Hegewald, J., Sein, D., Wang, Q., and Jung,
704   T.: AWI AWI-CM1.1MR model output prepared for CMIP6 CMIP,
705   https://doi.org/10.22033/ESGF/CMIP6.359, 2018.

706   Semmler, T., Danilov, S., Gierz, P., Goessling, H. F., Hegewald, J., Hinrichs, C., Koldunov, N., Khosravi, N.,
707   Mu, L., Rackow, T., Sein, D. V., Sidorenko, D., Wang, Q., and Jung, T.: Simulations for CMIP6 With the
708   AWI Climate Model AWI-CM-1-1, J. Adv. Model. Earth Syst., 12, e2019MS002009,
709   https://doi.org/10.1029/2019MS002009, 2020.

710   Semmler, T., Danilov, S., Rackow, T., Sidorenko, D., Barbi, D., Hegewald, J., Sein, D., Wang, Q., and Jung,
711   T.: CMIP6_supplemental CMIP AWI AWI-CM-1-1-MR, https://doi.org/10.26050/WDCC/C6sCMAWAWM,
712   2022a.

713   Semmler, T., Danilov, S., Rackow, T., Sidorenko, D., Barbi, D., Hegewald, J., Sein, D., Wang, Q., and Jung,
714   T.: CMIP6_supplemental ScenarioMIP AWI AWI-CM-1-1-MR,
715   https://doi.org/10.26050/WDCC/C6sSPAWAWM, 2022b.

716   Taburet, G., Sanchez-Roman, A., Ballarotta, M., Pujol, M.-I., Legeais, J.-F., Fournier, F., Faugere, Y., and
717   Dibarboure, G.: DUACS DT2018: 25 years of reprocessed sea level altimetry products, Ocean Sci., 15,
718   1207–1224, https://doi.org/10.5194/os-15-1207-2019, 2019.

719   Thiria, S., Sorror, C., Archambault, T., Charantonis, A., Bereziat, D., Mejia, C., Molines, J.-M., and Crépon,
720   M.: Downscaling of ocean fields by fusion of heterogeneous observations using Deep Learning
721   algorithms, Ocean Model., 182, 102174, https://doi.org/10.1016/j.ocemod.2023.102174, 2023.

722   Wang, Q., Danilov, S., Sidorenko, D., Timmermann, R., Wekerle, C., Wang, X., Jung, T., and Schröter, J.:
723   The Finite Element Sea Ice-Ocean Model (FESOM) v.1.4: formulation of an ocean general circulation
724   model, Geosci. Model Dev., 7, 663–693, https://doi.org/10.5194/gmd-7-663-2014, 2014.

725   Wang, Y., Claus, M., Greatbatch, R. J., and Sheng, J.: Decomposition of the Mean Barotropic Transport in
726   a High-Resolution Model of the North Atlantic Ocean, Geophys. Res. Lett., 44, 11,537-11,546,
727   https://doi.org/10.1002/2017GL074825, 2017.

728   van Westen, R. M. and Dijkstra, H. A.: Ocean eddies strongly affect global mean sea-level projections,
729   Sci. Adv., 7, eabf1674, https://doi.org/10.1126/sciadv.abf1674, 2021.

730   Yu, X., Ponte, A. L., Lahaye, N., Caspar-Cohen, Z., and Menemenlis, D.: Geostrophy Assessment and
731   Momentum Balance of the Global Oceans in a Tide- and Eddy-Resolving Model, J. Geophys. Res. Oceans,
732   126, e2021JC017422, https://doi.org/10.1029/2021JC017422, 2021.

733